

# Novel Fe hydrides and magnetism in the Fe-H system at high pressures

Ilya Kupenko (✉ [kupenko@wwu.de](mailto:kupenko@wwu.de))

University of Münster <https://orcid.org/0000-0003-3783-8360>

Elena Bykova

Photon Science, Deutsches Elektronen-Synchrotron <https://orcid.org/0000-0001-8652-024X>

Denis M. Vasiukov

University of Bayreuth

Georgios Aprilis

ESRF <https://orcid.org/0000-0002-0020-9125>

Valerio Cerantola

European XFEL GmbH

Aleksandr Chumakov

ESRF-The European Synchrotron <https://orcid.org/0000-0002-0755-0422>

Jeroen Jacobs

ESRF <https://orcid.org/0000-0002-7924-3851>

Maxim Bykov

Howard University <https://orcid.org/0000-0003-0248-1728>

Egor Koemets

Universität Bayreuth

Stella Chariton

University of Chicago <https://orcid.org/0000-0001-5522-0498>

Carmen Sanchez-Valle

University of Münster

Leonid Dubrovinsky

Bayerisches Geoinstitut <https://orcid.org/0000-0002-3717-7585>

---

## Article

**Keywords:** metallic hydrides, magnetics, metal-hydrides

**Posted Date:** February 12th, 2021

**DOI:** <https://doi.org/10.21203/rs.3.rs-148484/v1>

**License:** © ⓘ This work is licensed under a Creative Commons Attribution 4.0 International License.

[Read Full License](#)

---

# Novel Fe hydrides and magnetism in the Fe-H system at high pressures

I. Kupenko<sup>1,\*</sup>, E. Bykova<sup>2,3</sup>, D.M. Vasiukov<sup>4,5</sup>, G. Aprilis<sup>4</sup>, V. Cerantola<sup>6</sup>, A.I. Chumakov<sup>6</sup>, J. Jacobs<sup>6</sup>, M. Bykov<sup>3</sup>, E. Koemets<sup>3</sup>, S. Chariton<sup>3</sup>, C. Sanchez-Valle<sup>1</sup> and L. Dubrovinsky<sup>3</sup>

<sup>1</sup>*Institut für Mineralogie, University of Münster, Corrensstr. 24, 48149 Münster, Germany*

<sup>2</sup>*Photon Science, Deutsches Elektronen-Synchrotron, Notkestrasse 85, 22607, Hamburg, Germany*

<sup>3</sup>*Bayerisches Geoinstitut, University of Bayreuth, D-95440, Bayreuth, Germany*

<sup>4</sup>*Material Physics and Technology at Extreme Conditions, Laboratory of Crystallography, University of Bayreuth, D-95440 Bayreuth, Germany*

<sup>5</sup>*Synchrotron Radiation Research, Lund University, Box 118, S-221 00 Lund, Sweden,*

<sup>6</sup>*ESRF-The European Synchrotron, CS 40220, 38043, Grenoble, Cedex 9, France*

\*Corresponding author: [kupenko@uni-muenster.de](mailto:kupenko@uni-muenster.de)

## Abstract

The structure and properties of metal-hydrides at extreme conditions is key to the understanding of hydrogen-storage technologies, high-temperature superconductivity, and the dynamics of planetary cores. Here we investigate the phase relations and magnetic properties of iron hydrides, including two novel FeH<sub>x</sub> compounds, up to 63 GPa and 1800 K by Synchrotron Mössbauer Source spectroscopy and single-crystal X-ray diffraction. We observe the formation of a novel monoclinic iron hydride phase Fe<sub>2</sub>H<sub>-3</sub> at 63 GPa and 1000 K, which breaks down to a stoichiometric hexagonal closed packed FeH phase upon decompression below 52 GPa at 300 K. The long-range magnetic order in the two newly-synthesized phases persists to higher pressures compared to the well-known double hexagonal closed packed and face-centered cubic phases of FeH. The formation of magnetic Fe-H phases with high hydrogen concentration may influence the magnetic behavior of planetary metallic cores.

## Introduction

Metallic hydrides have been intensely investigated over the past years owing to their potential as hydrogen-storage materials<sup>1</sup> and their link to high-temperature superconductors with critical temperatures even above room temperature<sup>2-5</sup>. Particularly, iron hydrides have been in the focus of geosciences as plausible candidate materials in the metallic cores of the Earth, Earth-like rocky planets<sup>6,7</sup>, and hydrogen-rich gas giants<sup>8</sup>. Hydrogen is nearly insoluble in iron at ambient conditions. Yet, its solubility increases dramatically with pressure, leading to the formation of the stoichiometric FeH phase with a double-hexagonal close-packed structure (dhcp) even at room temperature<sup>9</sup>. For a long time, close-packed structures were the only known iron hydride phases with a hydrogen-to-iron ratio below or equal to one<sup>10</sup>. Over the last decade, however, evolutionary algorithms and density functional theory calculations have predicted new superstoichiometric iron hydrides, including FeH<sub>2</sub>, FeH<sub>3</sub>, FeH<sub>4</sub>, FeH<sub>5</sub>, FeH<sub>6</sub>, FeH<sub>7</sub>, FeH<sub>8</sub>, Fe<sub>3</sub>H<sub>5</sub>, Fe<sub>3</sub>H<sub>8</sub>, Fe<sub>3</sub>H<sub>13</sub><sup>11-13</sup>. Some of these novel binary iron hydride phases, namely FeH<sub>2</sub>, FeH<sub>3</sub><sup>14</sup>, and most recently FeH<sub>5</sub><sup>15</sup>, have been synthesized and characterized *in situ* in high-pressure, high-

temperature synchrotron X-ray diffraction studies (Fig. 1). However, a large fraction of the pressure-temperature space remains unexplored to date.

Magnetism of iron hydrides is also of particular interest<sup>16</sup>. For instance, the hexagonal closed packed (hcp) structure of iron has shown to be nonmagnetic<sup>17</sup> or an extremely weak antiferromagnet<sup>18,19</sup>, while the dhcp iron hydride phase has a long-range magnetic order at the same pressure-temperature conditions<sup>20</sup>. Yet, another cubic closed-packed structure of iron hydride (hereafter referred to as fcc-FeH, Fig. 1), does not show long-range magnetic ordering<sup>21</sup>. Moreover, the data on pressure-induced magnetic transition in dhcp-FeH is currently controversial with a transition pressure ranging from 22 GPa to 65 GPa depending on the experimental technique<sup>16,20,22,23</sup>.

In this study, we investigate the stability of the Fe-H system and magnetic transitions in iron hydrides up to 65 GPa employing Synchrotron Mössbauer spectroscopy (SMS) and single-crystal X-ray diffraction. We report two novel magnetic iron hydrides – monoclinic  $\text{Fe}_2\text{H}_{\sim 3}$  and stoichiometric FeH with hcp structure (Fig. 1). The anomalies in Mössbauer data of dhcp-FeH suggest the presence of ferromagnetic-antiferromagnetic transition in this hydride.

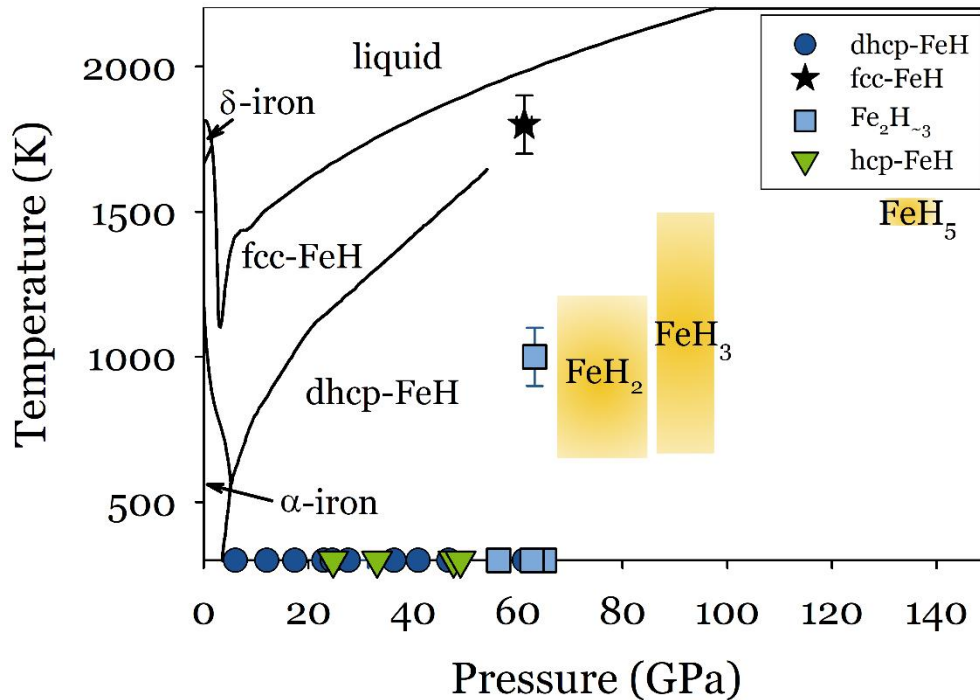


Figure 1. Phase diagram of the Fe-H system. The solid lines are the phase boundaries for the  $\text{FeH}_x$  phases with  $x \leq 1$ <sup>14,24,25</sup>, the shaded regions are the stability domains of the novel polyhydrides<sup>14,15</sup>. The symbols correspond to the phases investigated in this study, including the two new phases  $\text{Fe}_2\text{H}_{\sim 3}$  and hcp-FeH.

## Results and discussion

### Magnetic transitions in dhcp-FeH

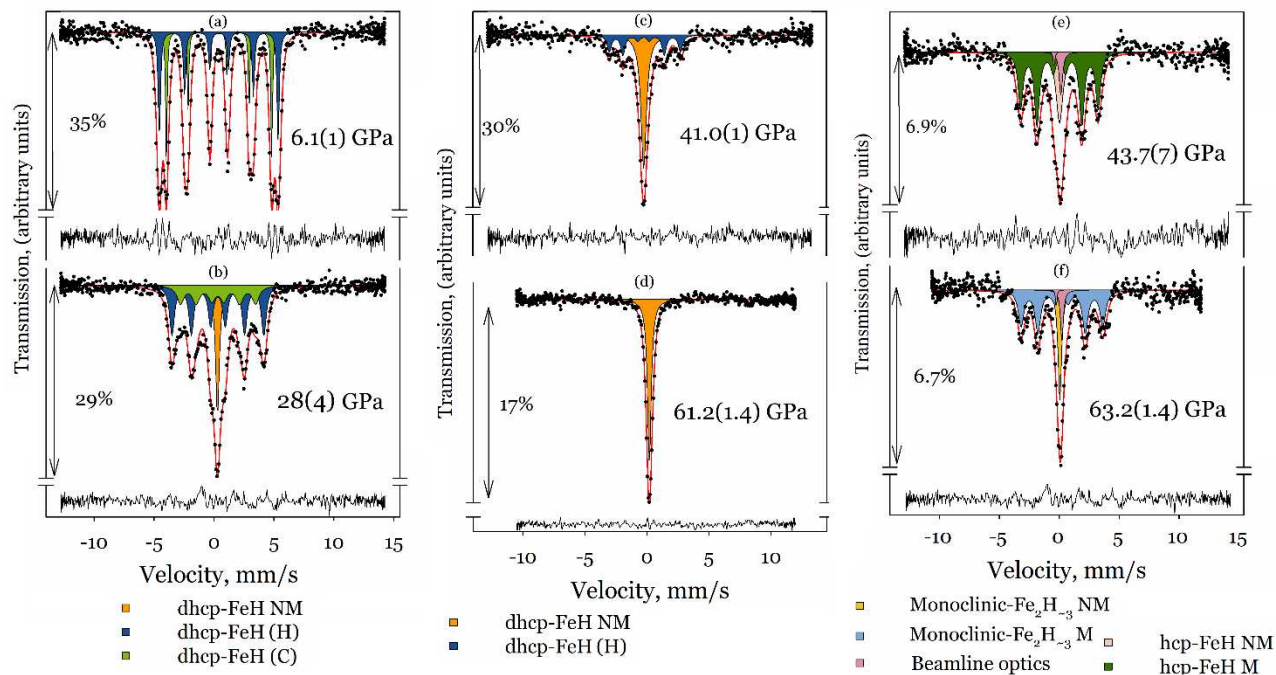


Figure 2. Representative SMS spectra of iron hydrides at the indicated pressures and ambient temperature. (a)-(d) – the cold compression of dhcp-FeH; (f) –  $\text{Fe}_2\text{H}_{-3}$  synthesized at about 1000 K; (e) hcp-FeH phase obtained upon decompression. Solid lines show the theoretical fits, the percentage bars indicate the relative absorptions, and the residuals of the fits are indicated below each spectrum. M: magnetic; NM: non-magnetic; H and C: hexagonally and cubically close-packed sites respectively.

Hydrogen incorporation into the iron structure remarkably affects its magnetic properties<sup>16</sup>. We collected Synchrotron Mössbauer Source (SMS) spectra of iron loaded with hydrogen upon compression up to 61.2(1.4) GPa at ambient temperature. At low pressures, the spectra can be fitted with a single magnetic contribution with hyperfine parameters corresponding to body-centered cubic  $\text{Fe}^{26}$ . Upon compression above 6 GPa the SMS spectrum characteristic for the double hexagonal closed pack structure iron hydride, FeH, arises (Fig. 2a). It consists of two well-resolved magnetic contributions with equal abundance owing to the two distinct crystallographic sites of Fe positions in the FeH dhcp structure<sup>20,27</sup>. The dhcp structure contains iron atoms with alternating cubic and hexagonal closed-packing order (ABAC), i.e. with iron sites resembling hexagonal closed packed and face-centered cubic local configurations, with octahedral interstitials between closest packed iron atoms occupied by hydrogen (Fig. 3a). The main difference between these sites is a coordination by hydrogen, with the octahedral and trigonal prismatic environment for cubic (c-site) and hexagonal (h-site) sites, respectively, and the difference in distance between hydrogen and iron layers. Hydrogen atoms are displaced from the centers of octahedral interstitials towards iron atoms in the cubic coordination<sup>28</sup>. Both iron sites have similar hyperfine parameters (Fig. 2a, table S1), although the site with a lower hyperfine magnetic field ( $B_{\text{hf}}$ ) has a systematically lower center shift (CS). The lower center shift corresponds to the higher electron density on the nuclei and, therefore, the site with lower CS corresponds to the atoms with the cubic close-packing

order. The same assignment was proposed in a previous Mössbauer study at ambient pressure and cryogenic temperatures based on the similarity between the hyperfine parameters of the site with higher  $B_{\text{hf}}$  and those of hexagonal closed packed cobalt hydride,  $\text{CoH}^{27}$ . The center shift and hyperfine magnetic field of both components decrease with increasing pressures (Fig. 4a, table S1).

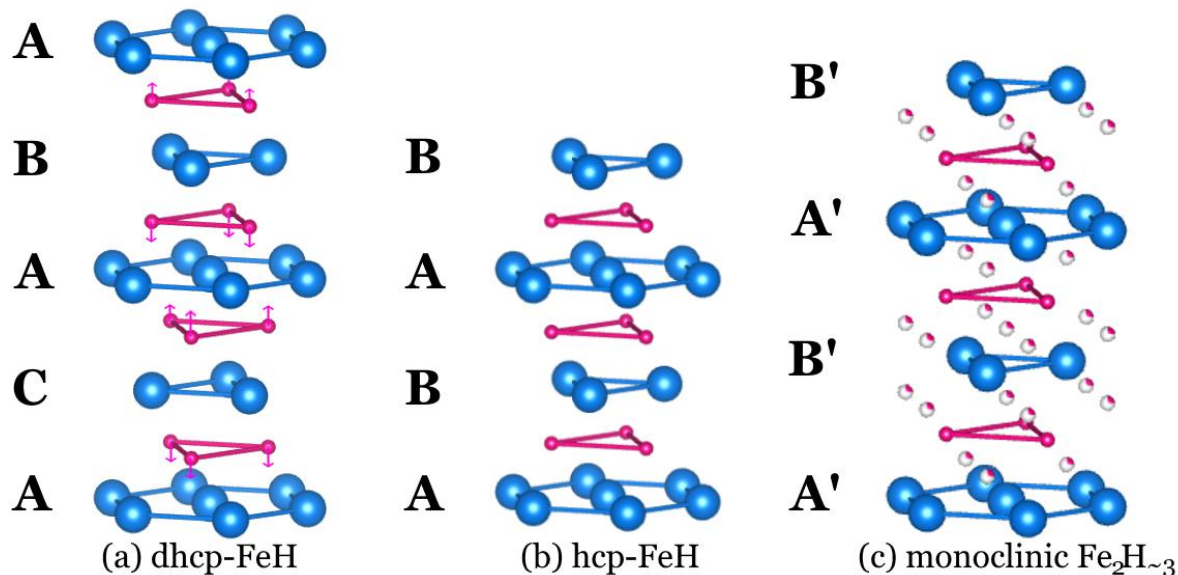


Figure 3. The crystal structures of iron hydrides. The blue and pink circles show regular positions of Fe and H atoms, respectively. The arrows indicate the directions of displacements of hydrogen atoms from the centers of octahedral interstices in the dhcp structure. The letters A, B, C represent the standard notation for close-packed layers in the dhcp- and hcp-FeH structures, A' and B' for the distorted close-packed layers in the monoclinic  $\text{Fe}_2\text{H}_{\sim 3}$  structure. In all three structures, all octahedral interstitials are occupied by hydrogen. In  $\text{Fe}_2\text{H}_{\sim 3}$ , additionally, about one-fourth of tetrahedral interstitials are occupied. The structures are visualized using the Vesta 3 software<sup>29</sup>.

Above 17 GPa, a new nonmagnetic component arises (Fig. 2b, Fig. 4b). Its relative abundance further increases with pressure at the expense of the magnetic component assigned to c-sites, which cannot be resolved above  $\sim 30$  GPa. Upon further compression, the relative abundance of the magnetic component assigned to h-sites starts to decrease, while the relative abundance of the paramagnetic singlet increases until it becomes the sole component in the spectra above  $\sim 55$  GPa (Fig. 2d). These observations are consistent with the results from a previous SMS study by Mitsui and Hirao<sup>20</sup>, which reported a residual weak hyperfine field decreasing sluggishly above 27.6 GPa and finally disappearing at 64.7 GPa. The coexistence of magnetically ordered and nonmagnetic contributions has been also observed in previous Nuclear Forward Scattering (NFS) studies, although the magnetic collapse was reported at about 30 GPa at room temperature<sup>22,30</sup>. The observed differences are unlikely caused by differences in stoichiometry. Badding et al.<sup>9</sup> showed that at high pressures and room temperature, even when an excess of iron is present, hydrogen tends to form stoichiometric dhcp-FeH, which coexists with unreacted iron, rather than forming a homogeneous non-stoichiometric compound. The coexistence of iron and stoichiometric dhcp-FeH at room temperature has been recently re-confirmed by X-ray and neutron diffraction measurements in  $\text{FeH}_{\sim 0.6}$  hydride<sup>31</sup>.

The magnetic transition in dhcp-FeH appears to be more complicated than an ordinary continuous ferromagnetic-paramagnetic transition. On one hand, x-ray magnetic circular dichroism (XMCD) measurements show a decrease of the integrated XMCD intensity and the collapse of the ferromagnetic state above around 30 GPa<sup>16,23</sup>, consistent with Nuclear Forward Scattering (NFS) investigations at room temperature<sup>22,30</sup>. On the other hand, the total local spin properties related to the local magnetic moments probed by Fe K $\beta$  x-ray emission spectroscopy (XES) gradually decrease with pressure and show an anomaly in relative weights of the ordered magnetic moments only above 43 GPa<sup>30</sup>. Moreover, the resistivity of the anomalous Hall effect, which is present in dhcp-FeH, decreases dramatically in the 25-30 GPa pressure range but does not reach zero, which indicates the magnetic order is not completely suppressed at high pressure<sup>30</sup>. The *ab initio* simulations show that the magnetic ordering temperature in dhcp-FeH crosses the room temperature only around 60 GPa<sup>32</sup>. The latter observations are in line with our data (Fig. 2c,d, Fig. 4a) and the earlier data of<sup>20</sup>. Furthermore, at temperatures below 200 K, the coexistence of magnetically ordered and paramagnetic contributions identified by the NFS technique persists to pressures above 50 GPa<sup>30</sup>.

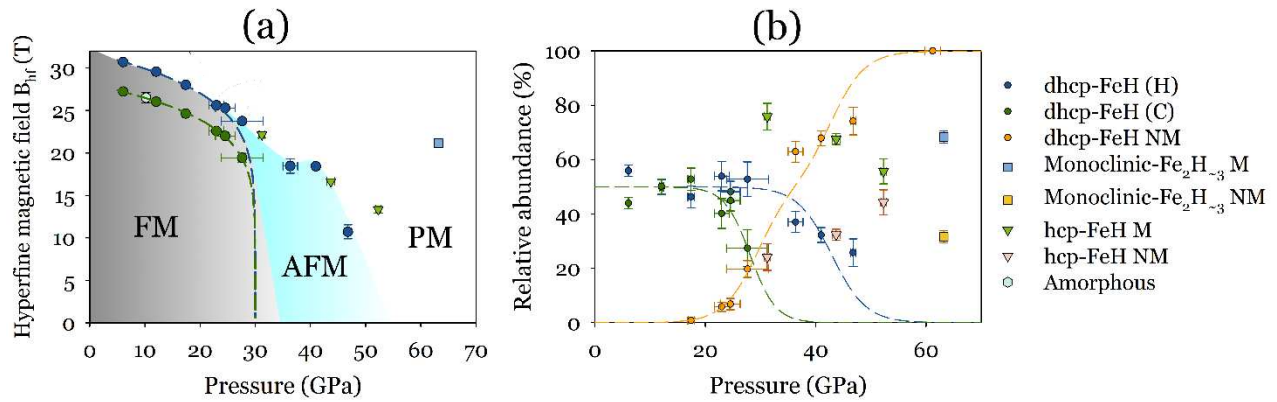


Figure 4. Effect of pressure on the hyperfine parameters of iron hydrides at room temperature: (a) hyperfine magnetic field, (b) relative abundance of the components. Dashed lines displayed in (a) are a fit to  $B_{hf}(P) = B_{hf_0} \left(1 - \frac{P}{P_c}\right)^\beta$  in the 0-35 GPa range and in (b) are guides for the eyes. The shaded areas in (a) indicate the ferromagnetic (FM), antiferromagnetic (AFM), and paramagnetic (PM) pressure regions for dhcp-FeH. M: magnetic; NM: non-magnetic; H and C: hexagonally and cubically close-packed sites respectively.

The coexistence of nonmagnetic and magnetically ordered sites within the same substance across a large pressure range observed here (Fig. 2b,c, Fig. 4b) and in refs.<sup>20,30</sup> is very unlikely in ferromagnetic materials with extremely similar environments of the crystallographic sites, such as in dhcp-FeH (Fig. 3a). We, therefore, suggest that the discrepancies in the magnetic behavior of dhcp-FeH are related to a pressure-induced ferromagnetic-antiferromagnetic transition<sup>33</sup>. It is evident that the hyperfine magnetic field on c-sites decreases faster than that on h-sites and it cannot be resolved above about 30 GPa (Fig. 2c, Fig. 4a). The hyperfine magnetic field on h-sites exhibits a sudden kink above 35 GPa (Fig. 4a). The discontinuous change of the  $B_{hf}$  is also observed across one of the best-known ferromagnetic-antiferromagnetic transitions in Fe-Rh alloys<sup>34</sup>. If the magnetic moments of the h-sites arrange in an antiferromagnetic order after 30 GPa, their influence on the c-sites would be canceled so that c-sites become paramagnetic. The ferromagnetic-antiferromagnetic transition would explain the absence of the XMCD signal in dhcp-FeH above 30 GPa<sup>16,23</sup>, while the residual magnetic signature will be still consistent with the XES<sup>30</sup>, earlier

SMS<sup>20</sup>, and our data (Fig. 2c, Fig. 4a), as well as with the reported anomalous Hall effect<sup>30</sup>. The SMS technique is indeed more sensitive to the presence of components with low relative abundance compared to the NFS technique. The room temperature Mössbauer spectrum in the 30-50 GPa range is dominated by the nonmagnetic component and thus, the magnetic contribution could be easily overlooked by NFS<sup>22,30</sup>, but clearly detected by SMS (Fig. 2c).

### Formation of the novel Fe<sub>2</sub>H<sub>~3</sub> phase at high temperatures

Laser heating of dhcp-FeH at 61.2(1.4) GPa and 1800(100) K for several minutes (Fig. 1) resulted in the appearance of a nonmagnetic component with a slightly increased center shift relative to dhcp-FeH (table S1). We attribute this change to the formation of face-centered cubic FeH<sup>21</sup>. Further heating of fcc-FeH at moderate temperature, ~ 1000(100) K, and 63.2(1.4) GPa for about half an hour results in the formation of a new iron hydride (Fig. 1). Our X-ray diffraction data show that the new compound formed as several single-crystal twin domains that were preserved upon temperature quench. The powder profile refinement yields a monoclinic unit cell with space group C2/m with a small deviation of  $\beta$  angle from 90 degrees (Fig. 5a, Table S2). The structure differs from that of Fe<sub>3</sub>H<sub>5</sub> and Fe<sub>3</sub>H<sub>8</sub> phases predicted to be stable at this pressure<sup>11</sup>, and it is a monoclinic distortion of the hcp structure. The presence of other Fe-containing phases was not observed in the sample.

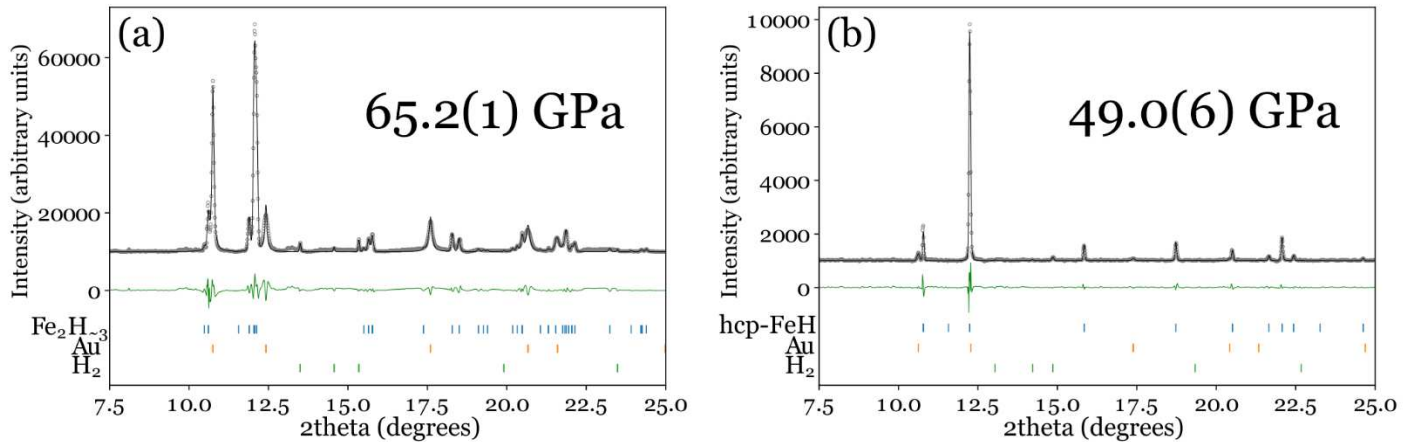


Figure 5. X-ray diffraction patterns of (a) monoclinic Fe<sub>2</sub>H<sub>~3</sub> (space group C2/m) and (b) hcp-FeH GPa at indicated pressures and room temperature. Experimental data – grey circles; Le Bail fit – black solid lines; difference curves – green solid lines. Ticks show predicted positions of the diffraction peaks. The wavelength is 0.4126 Å.

The volume per iron atom in the new Fe hydride at 65.1(2) GPa and room temperature is 11.741(3) Å<sup>3</sup>, which is much higher than that of dhcp-FeH at similar conditions (Fig. 6). This is likely due to the expansion of the structure due to further hydrogenation. The low scattering power of hydrogen atoms prevents the determination of their positions and consequently the stoichiometry using X-ray diffraction. The amount of hydrogen in iron hydrides,  $x$ , can be estimated using the formula<sup>7,21,31</sup>:

$$x = \frac{V_{FeH_x} - V_{Fe}}{\Delta V_H}, \quad (1)$$

where  $V_{FeHx}$  and  $V_{Fe}$  are the atomic volumes of iron hydride and pure iron respectively, and  $\Delta V_H$  is the atomic volume expansion caused by the incorporation of one atom of interstitial hydrogen. Furthermore, we employed the equations of state of pure hcp iron<sup>35</sup> and stoichiometric dhcp-FeH<sup>14</sup> to calculate the pressure dependence of  $\Delta V_H$  (Fig. 6). We determined  $\Delta V_H = 1.66 \text{ \AA}^3$  at 65.1(2) GPa and used this value in Eq.(1) to determine hydrogen content  $x$  in the novel monoclinic iron hydride. Our calculations yield  $x \approx 1.61(5)$ , corresponding to the chemical formula  $Fe_2H_{\sim 3}$  for the new phase.

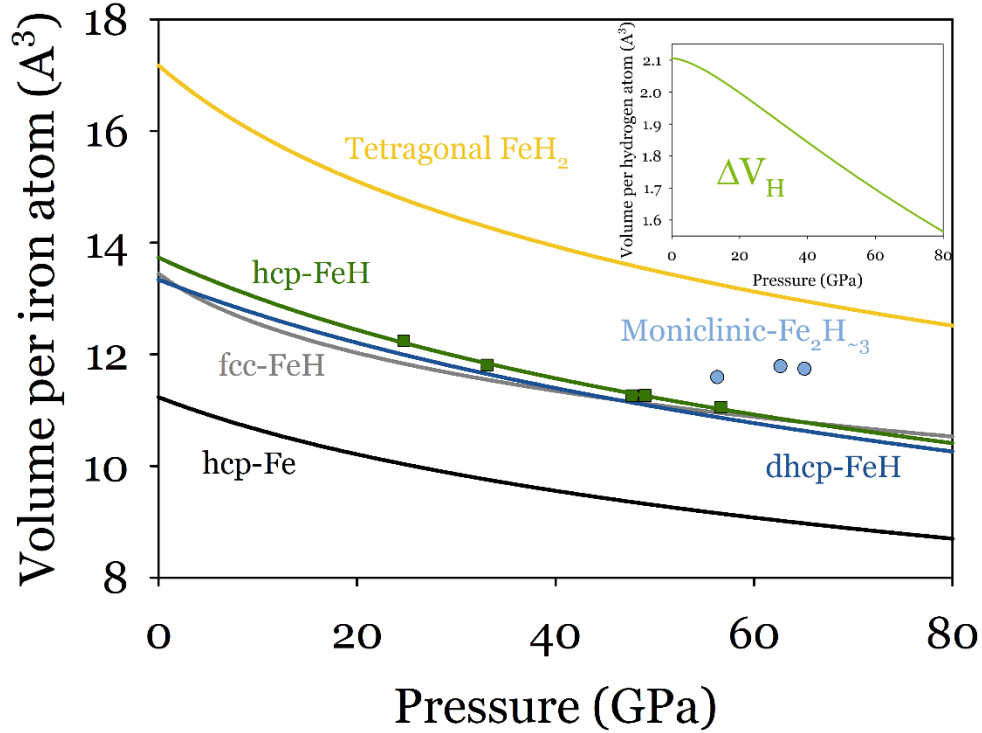


Figure 6. Third-order Birch–Murnaghan equations of state for hcp-FeH (green, this study), hcp-Fe (black)<sup>35</sup>, dhcp-FeH (blue), and tetragonal  $FeH_2$  (yellow)<sup>14</sup>, together with P-V data for monoclinic- $Fe_2H_{\sim 3}$  (light-blue circles). Error bars do not exceed the size of the symbols. The EOS parameters are given in Supplementary Table 3. The inset shows the calculated atomic volume expansion caused by the incorporation of one atom of interstitial hydrogen according to Eq. (1).

The SMS spectrum of the new hydride can be fitted by two components – one magnetically ordered and another nonmagnetic (Fig. 2f). Unlike in the original dhcp structure, the CS of the two components is significantly different (Table S1), indicating a distinct atomic environment, particularly the electron density. The increase of CS of the magnetic component relative to dhcp-FeH can be well explained by the expansion of the crystal lattice (Fig. 6, Fig. 7). The relatively low CS of the non-magnetic component, in turn, should be related to the increase of the electron density on the nuclei. In an ideal closed packed structure, there is one octahedral interstitial per close-packed atom, so that every octahedral interstitial in stoichiometric FeH is occupied by one hydrogen atom. If the hydrogen content is higher than one, however, hydrogen should occupy the remaining tetrahedral interstitials. Our estimates of hydrogen content indicate that  $\sim 1/4$  of tetrahedral interstitials in the new distorted hcp structure are occupied by hydrogen (Fig. 3c). As there are 8 tetrahedral interstitials around each Fe atom the average coordination number should increase by  $\frac{1}{4} \times 8 = 2$ . Since two different iron environments are identified, with an

approximate ratio of 2:1 between the two sites (Fig. 4b, Table S1), we assume that the coordination number of  $\sim 2/3$  iron atoms remains unchanged, while the coordination number of  $1/3$  of the atoms increases from 6 to 12. This change of the coordination number of a fraction of iron atoms increases their electron density due to electrons donated by hydrogen and consequently decreases the CS. Such a distinct division between two types of iron sites is plausible because density functional theory calculations have shown the tendency of H atoms to segregate into layers even for a low Fe/H ratio in the hcp-structure<sup>12</sup>. For higher hydrogen contents, the presence of  $\text{FeH}_{12}$  icosahedral units has been predicted<sup>12</sup> and 12- and 13-coordinated iron has been observed in  $\text{FeH}_3$  and  $\text{FeH}_5$  compounds, respectively<sup>14,15</sup>.

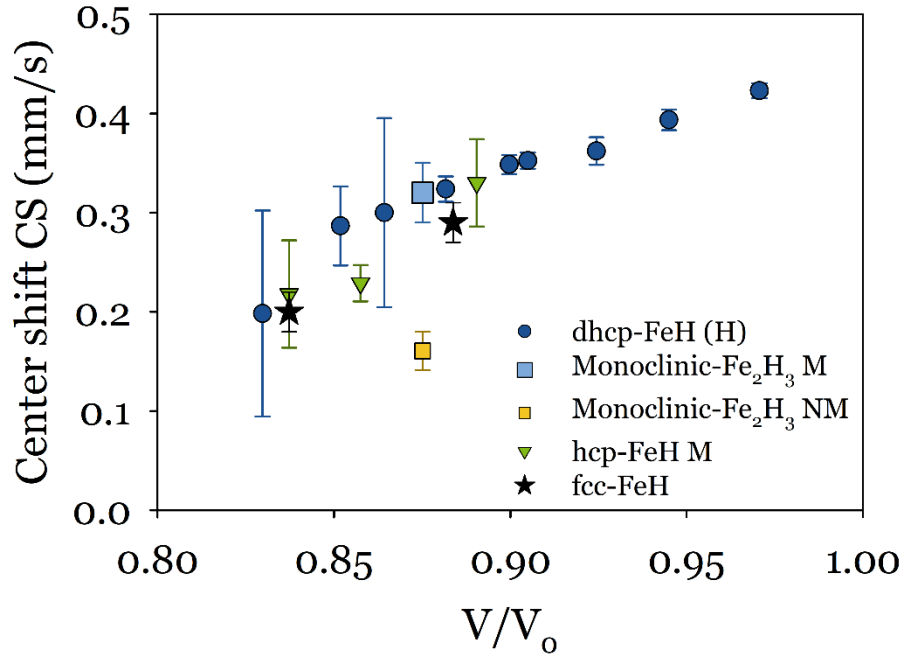


Figure 7. Volume dependence of the center shift in dhcp-FeH (blue), hcp-FeH (green), and monoclinic  $\text{Fe}_2\text{H}_{-3}$ . The effect of volume increase well explains the higher CS of the magnetic component in  $\text{Fe}_2\text{H}_{-3}$  (light blue) but does not explain the low-CS of the nonmagnetic component (yellow). Volumes of dhcp-FeH are calculated using the EoS parameters reported in Supplementary Table 2. The data for fcc-FeH are from<sup>21</sup>.

The magnetic behavior of the novel iron hydride could be qualitatively explained based on the Stoner criterion for itinerant magnetism<sup>36</sup>:

$$I\mathcal{D}(E_F) \geq 1, \quad (2)$$

where  $I$  is the molecular field constant, which is not sensitive to pressure, and  $\mathcal{D}(E_F)$  the density of states (DOS) at the Fermi level in the nonmagnetic state. If the Stoner criterion [Eq. (2)] is fulfilled, then spin-polarization, i.e. long-range magnetic order, occurs. Hydrogenation acts on the magnetic properties of iron in two major ways. First, it causes the narrowing of the electronic bands due to the reduced overlap between iron 3d orbitals following volume expansion. Second, hydrogen incorporation shifts the 3d band with respect to  $E_F$  due to the electrons donated to the Fe-atom and the creation of the new electronic states at low energy with respect to the Fermi level<sup>16,37</sup>. In the dhcp structure, and at low pressures, the Stoner criterion [Eq. (2)] is fulfilled and the majority-spin 3d band of DOS is almost full. Pressure increase results in the broadening of the electronic band due to volume collapse and its shift to energies above

$E_F$ <sup>16</sup>. This is accompanied by partial filling of the minority-spin 3d band and a decrease of the magnetic moment until the collapse of the magnetic order. Temperature-induced hydrogenation and structural transition to Fe<sub>2</sub>H<sub>~3</sub> leads to the further narrowing of the electronic bands so that Eq. (2) is fulfilled again for the 6-hydrogen coordinated iron atoms. Any added d electrons would reduce the magnetic moments because they would likely go into the minority band which presumably has a higher density of states at the Fermi level<sup>38</sup>. Therefore, additional electrons, donated by hydrogen to 12-hydrogen coordinated iron atoms should put  $E_F$  above the 3d band of Fe, i.e the DOS at  $E_F$  is low, similarly to nonmagnetic NiH<sup>16</sup>, and Stoner criterion [Eq. (2)] is not fulfilled.

Interestingly, the temperature increase does not cause a decrease in the magnetic field  $B_{hf}$  (Fig. S3), table S1). This indicates that the temperature-induced decrease of  $B_{hf}$  is likely compensated by the distortion and expansion of the structure upon further incorporation of hydrogen. The indirect evidence of higher hydrogen content at high temperature is provided by the behavior of CS: while the temperature of 1000 K should decrease the CS of Mössbauer components by  $\sim 0.5$  mm/s<sup>39</sup>, a very moderate decrease by  $\sim 0.15$  mm/s for the magnetic component and almost no change of the CS of the nonmagnetic component are observed. Such behavior is consistent with the expansion of the lattice due to further hydrogen incorporation.

### Breakdown of Fe<sub>2</sub>H<sub>~3</sub> into hcp-FeH phase upon decompression

Further, we performed decompression experiments of the Fe<sub>2</sub>H<sub>~3</sub> compound at room temperature (Fig. 1). The phase remains stable down to 56.3(3) GPa (space group C2/m), although the unit-cell volume slightly decreases upon decompression. This observation could be explained by the gradual reduction of the hydrogen amount. Upon further decompression, the transition to the hcp structure occurs (Fig. 3b, Fig. 5b) and it is accompanied by a significant reduction of the unit cell volume (Fig. 6, table S2). By applying Eq.(1), the hydrogen content in the new phase is determined to be 1.09(4), i.e. close to stoichiometry FeH. The phase hcp-FeH<sub>x</sub> has been observed before at relatively low pressures as a paramagnetic phase but only for hydrogen contents of  $x \sim 0.3-0.6$ <sup>10,28,31</sup>. Stoichiometric magnetically ordered hcp-FeH was theoretically predicted to be the stable phase in the 37-83 pressure range<sup>40</sup>, but to the best of our knowledge, this is the first experimental observation of this phase. The pressure-volume data of hcp-FeH was fitted by the second-order Birch-Murnaghan equation of state to retrieve the volume at zero pressure and the bulk modulus (Table S2). Below 24.7(1) GPa the diffraction signal from hcp-FeH disappeared suggesting amorphization of the sample (Fig. S3). Interestingly, decompression of dhcp-FeH and non-stoichiometric hcp-FeH does not lead to amorphization of the sample, but rather to the formation of body-centered cubic iron<sup>31,38</sup>.

The breakdown of Fe<sub>2</sub>H<sub>~3</sub> into stoichiometric hcp-FeH upon decompression results in a noticeable change of the SMS spectrum (Fig. 2e). The spectrum of hcp-FeH can be fitted with two contributions, one magnetically ordered and one non-magnetic, with similar CS (Table S1). Similar to dhcp-FeH, further decompression increases the relative abundance of the magnetic component and the  $B_{hf}$  without abrupt changes down to 31.2(5) GPa (Fig. 4). The hcp structure has only one nonequivalent iron site with hydrogen located in the center of the octahedral interstitials<sup>31</sup>. Therefore, we attribute the coexistence of magnetic and non-magnetic components within the same iron site to relaxation effects related to the nature of the Mössbauer technique when the characteristic time of the spin flips is of the order of the Larmor period<sup>41-44</sup>. We note that the same effect is likely responsible for the coexistence of magnetic and

non-magnetic components from the same site in dhcp-FeH (Fig. 2b), but cannot explain such coexistence arising from different sites (Fig. 2c).

There is a remarkable difference in the magnetic properties of dhcp-FeH and hcp-FeH at high pressures. At 52.3(5) GPa hcp-FeH still retains the long-range magnetic order, unlike its dhcp polymorph (Fig. 2d, 2e). The unit cell volumes of both polymorphs are similar at high pressures (Fig. 5) as are the center shifts of magnetic and nonmagnetic components (Fig. 7, table S1). Thus, the difference in magnetic properties can only be due to differences in their density of states, DOS, around the Fermi level. Indeed, first-principles calculations suggest that the Fermi level lays still at the majority-spin 3d band of hcp-FeH at 55 GPa, and filling of the minority spin band and proceeding collapse of magnetism happens only at higher pressures<sup>45</sup>. Our data anticipate that the collapse of the magnetic order should occur above 60 GPa (Fig. 4a). This observation concurs with theoretical studies suggesting the persistence of the magnetic order in the hcp structure to higher pressures than in the dhcp structure<sup>45-47</sup>.

## Conclusion

The phase relations and magnetic transitions in the Fe-H system have been investigated up to 63 GPa and 1800 K in laser-heated diamond-anvil cells by Synchrotron Mossbauer Spectroscopy (SMS) and X-ray diffraction. We report the synthesis of two novel Fe hydrides, monoclinic Fe<sub>2</sub>H<sub>3</sub> at 63 GPa and stoichiometric hcp-FeH below 52 GPa, which add to the complexity of the phase diagram of the Fe-H system (Fig. 1). Further detailed investigations of the magnetic transitions in dhcp-FeH suggest that the collapse of the magnetic order proceeds in two steps: firstly, as a ferromagnetic-antiferromagnetic transition around 30 GPa and secondly, as an antiferromagnetic-paramagnetic transition around 50 GPa.

The present study suggests a larger diversity of iron hydride phases in yet unexplored pressure-temperature domains. The persistence of magnetism in hcp-FeH at high pressures and the formation of hydrogen-rich magnetic phases may play an important role in the magnetic behavior of the smaller planetary bodies, whose interior can have temperatures below the Curie temperature of iron hydrides. The persistent magnetism at high pressure may affect the predicted superconductivity of iron hydrides<sup>11,15</sup>. These observations should stimulate the quest for additional (and unconventional) iron hydrides and the study of their magnetic properties.

## Methods

**Sample preparation.** All experiments were performed on membrane-type diamond anvil cells<sup>48</sup>. Diamonds with 250  $\mu\text{m}$  culets were employed to reach pressures above 60 GPa at 1800 K. Compression chambers were prepared from 200  $\mu\text{m}$  thick Re gaskets pre-indented to about 30  $\mu\text{m}$  thickness and laser-drilled with a hole of 125  $\mu\text{m}$ . The gaskets were lined with an Au ring to prevent chemical reactions and H<sub>2</sub> embrittlement<sup>49</sup>. The Au-lined gaskets were prepared from an Au foil indented into the sample chamber and drilled with a hole of about 100  $\mu\text{m}$ , forming a 15  $\mu\text{m}$  deep recess to host the sample and ensure chemical insulation from the diamonds (Fig. S1). Isotopically pure (95% enrichment) <sup>57</sup>Fe foils of 1  $\mu\text{m}$  thickness were loaded onto the gasket together with several small ruby chips for pressure determination<sup>50</sup>. H<sub>2</sub> was loaded at 1.2 kbar and serves both as the reaction and as a pressure transmitting medium as well as a thermal insulator.

**Mössbauer spectroscopy at extreme conditions.** SMS spectra were recorded at the Nuclear Resonance Beamline<sup>51</sup> ID18 of the European Synchrotron Radiation Facility (ESRF, Grenoble, France) using the (111)

nuclear reflection of a  $^{57}\text{FeBO}_3$  single crystal mounted on a Wissel velocity transducer driven with a sinusoidal waveform<sup>52</sup>. The source provides  $^{57}\text{Fe}$  resonant radiation at 14.4 keV within a bandwidth of 15 neV (0.31 mm/s) which is tunable in energy. The X-ray beam was focused down to  $16 \times 12 \mu\text{m}^2$  (VxH) employing Kirkpatrick-Baez mirrors. The linewidth of the SMS and the absolute position of the center shift (CS) relative to  $\alpha$ -iron were controlled before and after each measurement with a  $\text{K}_2\text{Mg}^{57}\text{Fe}(\text{CN})_6$  reference single line absorber. The velocity scale was calibrated using 25  $\mu\text{m}$  thick natural iron foil. High-temperature measurements were performed with a modified version of the portable double-sided laser-heating system described in ref. [53]. Two infrared fiber lasers operating at 1070 nm were focused down to  $\sim 40 \mu\text{m}$  (full width at a half maximum) at the sample position. The surface temperature was measured by the standard spectroradiometry method employing an IsoPlane SCT 320 spectrometer with a PI-MAX<sup>®</sup>4 1024i ICCD camera from Princeton Instruments<sup>54</sup>. Typical collection times ranged from 30 minutes to 8 hours depending on pressure and the desired statistics. SMS spectra were fitted using a transmission integral with a normalized Lorentzian-squared source line shape using the MossA software package<sup>55</sup>.

**Single crystal X-ray diffraction.** The single-crystal X-ray diffraction measurements were conducted on the ID15B beamline at ESRF using a monochromatic beam of  $\lambda=0.4126 \text{ \AA}$  and a MAR555-image plate detector for collection. Sample-to-detector distance, coordinates of the beam center, tilt angle, and tilt plane rotation angle of the detector images were calibrated using Si powder. At each pressure step, the X-ray diffraction (XRD) images were collected upon continuous rotation of the cell from  $-32^\circ$  to  $+32^\circ \omega$ ; while data collection experiments were performed by narrow  $0.5^\circ$  scanning of the same omega range. Pressures were calculated from the lattice parameters of Au<sup>56</sup> refined from the XRD patterns recorded in the gasket liner (Fig. S1).

Diffraction data analysis (peak search, unit cell indexing, data integration, frame scaling, etc.) was performed with the CrysAlis<sup>Pro</sup> software. A single crystal of an orthoenstatite ( $(\text{Mg}_{1.93}, \text{Fe}_{0.06})(\text{Si}_{1.93}, \text{Al}_{0.06})\text{O}_6$ , *Pbca*,  $a = 18.2391(3) \text{ \AA}$ ,  $b = 8.8117(2) \text{ \AA}$ ,  $c = 5.18320(10) \text{ \AA}$ ), was used to calibrate the instrument model of CrysAlis<sup>Pro</sup> software (sample-to-detector distance, the origin of the detector, offsets of the goniometer angles and rotation of the X-ray beam and the detector around the instrument axis).

Due to the strong overlap between reflections no decent integration using CrysAlis software was possible above 56 GPa. In order to address this problem and determine the correct space group, we integrated XRD wide images into 1-dimensional powder patterns. Then, using JANA2006<sup>57</sup> software we generated distorted crystal structures of hcp structure and compared the experimental powder profiles with calculated positions of the reflections corresponding to different subgroups. Below 56 GPa the crystal structure was determined by the dual space method using SHELXT<sup>58</sup> software. After the structure solution, the position of an iron atom was found while the positions of hydrogen atoms were not determined due to its low scattering power. The crystal structures were refined against  $F^2$  on all data by full-matrix least-squares with the SHELXL<sup>59</sup> software. The final unit cell parameters of the structures were refined with the use of the Le Bail fitting of the powder patterns.

## Data availability

Data generated during the study are available in the repository <https://unimuenster.sciebo.de/s/kZyNiftW2GGusEN>.

## References

1. Schlapbach, L. & Züttel, A. Hydrogen-storage materials for mobile applications. *Nature* **414**, 353–358 (2001).
2. Grockowiak, A. D. *et al.* Hot Hydride Superconductivity above 550 K. (2020).
3. Drozdov, A. P. *et al.* Superconductivity at 250 K in lanthanum hydride under high pressures. *Nature* **569**, 528–531 (2019).
4. Zurek, E., Hoffmann, R., Ashcroft, N. W., Oganov, A. R. & Lyakhov, A. O. A little bit of lithium does a lot for hydrogen. *Proc. Natl. Acad. Sci.* **106**, 17640–17643 (2009).
5. Pickard, C. J., Errea, I. & Eremets, M. I. Superconducting Hydrides Under Pressure. *Annu. Rev. Condens. Matter Phys.* **11**, 57–76 (2020).
6. Caracas, R. The influence of hydrogen on the seismic properties of solid iron. *Geophys. Res. Lett.* **42**, 3780–3785 (2015).
7. Shibazaki, Y. *et al.* Sound velocity measurements in dhcp-FeH up to 70GPa with inelastic X-ray scattering: Implications for the composition of the Earth's core. *Earth Planet. Sci. Lett.* **313–314**, 79–85 (2012).
8. Wahl, S. M., Wilson, H. F. & Militzer, B. Solubility of iron in metallic hydrogen and stability of dense cores in giant planets. *Astrophys. J.* **773**, 95 (2013).
9. Badding, J. V., Hemley, R. J. & Mao, H. K. High-Pressure Chemistry of Hydrogen in Metals: In Situ Study of Iron Hydride. *Science* **253**, 421–424 (1991).
10. Yamakata, M., Yagi, T., Utsumi, W. & Fukai, Y. In situ X-ray Observation of Iron Hydride under High Pressure and High Temperature. *Proc. Japan Acad. Ser. B Phys. Biol. Sci.* **68**, 172–176 (1992).
11. Kvashnin, A. G., Kruglov, I. A., Semenok, D. V. & Oganov, A. R. Iron Superhydrides FeH<sub>5</sub> and FeH<sub>6</sub> : Stability, Electronic Properties, and Superconductivity. *J. Phys. Chem. C* **122**, 4731–4736 (2018).
12. Bazhanova, Z. G., Oganov, A. R. & Gianola, O. Fe–C and Fe–H systems at pressures of the Earth's inner core. *Physics-Uspokhi* **55**, 489–497 (2012).
13. Zarifi, N., Bi, T., Liu, H. & Zurek, E. Crystal Structures and Properties of Iron Hydrides at High Pressure. *J. Phys. Chem. C* **122**, 24262–24269 (2018).
14. Pépin, C. M., Dewaele, A., Geneste, G. & Loubeyre, P. New Iron Hydrides under High Pressure. *Phys. Rev. Lett.* **265504**, 1–5 (2014).
15. Pépin, C. M., Geneste, G., Dewaele, A., Mezouar, M. & Loubeyre, P. Synthesis of FeH<sub>5</sub>: A layered structure with atomic hydrogen slabs. *Science* **357**, 382–385 (2017).
16. Ishimatsu, N. *et al.* Hydrogen-induced modification of the electronic structure and magnetic states in Fe, Co, and Ni monohydrides. *Phys. Rev. B* **86**, 104430 (2012).
17. Cort, G. Search for magnetism in hcp  $\epsilon$ -Fe. *J. Appl. Phys.* **53**, 2064 (1982).
18. Ohno, H. Antiferromagnetism in hcp Iron-Ruthenium and hcp Iron-Osmium Alloys. *J. Phys. Soc. Japan* **31**, 92–101 (1971).

19. Bessas, D. *et al.* Revealing the hidden hyperfine interactions in  $\epsilon$ -iron. *Phys. Rev. B* **101**, 035112 (2020).
20. Mitsui, T. & Hirao, N. Ultrahigh-pressure study on the magnetic state of iron hydride using an energy domain synchrotron radiation  $^{57}\text{Fe}$  Mössbauer spectrometer. *MRS Proc.* **1262**, 1262-W06-09 (2010).
21. Narygina, O. *et al.* X-ray diffraction and Mössbauer spectroscopy study of fcc iron hydride FeH at high pressures and implications for the composition of the Earth's core. *Earth Planet. Sci. Lett.* **307**, 409–414 (2011).
22. Mao, W. L. Nuclear resonant x-ray scattering of iron hydride at high pressure. *Geophys. Res. Lett.* **31**, L15618 (2004).
23. Bouldi, N., Sainctavit, P., Juhin, A., Nataf, L. & Baudalet, F. Electronic and magnetic properties of iron hydride under pressure: An experimental and computational study using x-ray absorption spectroscopy and x-ray magnetic circular dichroism at the Fe K edge. *Phys. Rev. B* **98**, 064430 (2018).
24. Sakamaki, K. *et al.* Melting phase relation of  $\text{FeH}_x$  up to 20 GPa: Implication for the temperature of the Earth's core. *Phys. Earth Planet. Inter.* **174**, 192–201 (2009).
25. Hirose, K. *et al.* Hydrogen Limits Carbon in Liquid Iron. *Geophys. Res. Lett.* **46**, 5190–5197 (2019).
26. Pipkorn, D. N. *et al.* Mössbauer Effect in Iron under Very High Pressure. *Phys. Rev.* **135**, A1604–A1612 (1964).
27. Schneider, G. *et al.* Mössbauer study of hydrides and deuterides of iron and cobalt. *J. Less Common Met.* **172–174**, 333–342 (1991).
28. Antonov, V. *et al.* Neutron diffraction investigation of the dhcp and hcp iron hydrides and deuterides. *J. Alloys Compd.* **264**, 214–222 (1998).
29. Momma, K. & Izumi, F. VESTA 3 for three-dimensional visualization of crystal, volumetric and morphology data. *J. Appl. Crystallogr.* **44**, 1272–1276 (2011).
30. Ying, J. *et al.* Magnetic phase diagram of  $\epsilon'$ -FeH. *Phys. Rev. B* **101**, 2–6 (2020).
31. Machida, A. *et al.* Hexagonal Close-packed Iron Hydride behind the Conventional Phase Diagram. *Sci. Rep.* **9**, 12290 (2019).
32. Gomi, H., Fei, Y. & Yoshino, T. The effects of ferromagnetism and interstitial hydrogen on the equation of states of hcp and dhcp  $\text{FeH}_x$ : Implications for the Earth's inner core age. *Am. Mineral.* **103**, 1271–1281 (2018).
33. Wysokiński, M. M. Mechanism for transitions between ferromagnetic and antiferromagnetic orders in d-electron metallic magnets. *Sci. Rep.* **9**, 1–8 (2019).
34. Shirane, G., Chen, C. W., Flinn, P. A. & Nathans, R. Mössbauer Study of Hyperfine Fields and Isomer Shifts in the Fe-Rh Alloys. *Phys. Rev.* **131**, 183–190 (1963).
35. Dewaele, A. *et al.* Quasihydrostatic Equation of State of Iron above 2 Mbar. *Phys. Rev. Lett.* **97**, 215504 (2006).
36. Stoner, E. Collective electron ferromagnetism. *Proc. R. Soc. London. Ser. A. Math. Phys. Sci.* **165**,

- 372–414 (1938).
37. León, A., Velásquez, E. A., Mejía-López, J. & Vargas, P. Ab initio study of the magnetic behavior of metal hydrides: A comparison with the Slater-Pauling curve. *Comput. Mater. Sci.* **141**, 122–126 (2018).
  38. Choe, I., Ingalls, R., Brown, J. M., Sato-Sorensen, Y. & Mills, R. Mössbauer studies of iron hydride at high pressure. *Phys. Rev. B* **44**, 1–4 (1991).
  39. Maradudin, A. A., Flinn, P. A. & Ruby, S. Velocity shift of the Mössbauer resonance. *Phys. Rev.* **126**, 9–23 (1962).
  40. Isaev, E. I., Skorodumova, N. V., Ahuja, R., Vekilov, Y. K. & Johansson, B. Dynamical stability of Fe-H in the Earth's mantle and core regions. *Proc. Natl. Acad. Sci.* **104**, 9168–9171 (2007).
  41. Levinson, L. M., Luban, M. & Shtrikman, S. Mössbauer Studies on Fe-57 near the Curie Temperature. *Phys. Rev.* **177**, 864–871 (1969).
  42. Yukalov, V. I. Phase transitions and heterophase fluctuations. *Phys. Rep.* **208**, 395–489 (1991).
  43. Rancourt, D. G. Pervasiveness of cluster excitations as seen in the Mössbauer spectra of magnetic materials. *Hyperfine Interact.* **40**, 183–194 (1988).
  44. van der Woude, F. & Dekker, A. J. The Relation between Magnetic Properties and the Shape of Mössbauer Spectra. *Phys. status solidi* **9**, 775–786 (1965).
  45. Tsumuraya, T., Matsuura, Y., Shishidou, T. & Oguchi, T. First-Principles Study on the Structural and Magnetic Properties of Iron Hydride. *J. Phys. Soc. Japan* **81**, 064707 (2012).
  46. Skorodumova, N. V., Ahuja, R. & Johansson, B. Influence of hydrogen on the stability of iron phases under pressure. *Geophys. Res. Lett.* **31**, 5–7 (2004).
  47. Kato, C. *et al.* Stability of fcc phase FeH to 137 GPa. *Am. Mineral.* **105**, 917–921 (2020).
  48. Letoullec, R., Pinceaux, J. P. & Loubeyre, P. The membrane diamond anvil cell: A new device for generating continuous pressure and temperature variations. *High Press. Res.* **1**, 77–90 (1988).
  49. Datchi, F., Loubeyre, P. & LeToullec, R. Melting Curves of Hydrogen, H<sub>2</sub>O, Helium and Argon at High Pressure. *Rev. HIGH Press. Sci. Technol.* **7**, 778–780 (1998).
  50. Dewaele, A., Torrent, M., Loubeyre, P. & Mezouar, M. Compression curves of transition metals in the Mbar range: Experiments and projector augmented-wave calculations. *Phys. Rev. B* **78**, 104102 (2008).
  51. Ruffer, R. & Chumakov, A. I. Nuclear Resonance Beamline at ESRF. *Hyperfine Interact.* **97–98**, 589–604 (1996).
  52. Potapkin, V. *et al.* The <sup>57</sup>Fe Synchrotron Mössbauer Source at the ESRF. *J. Synchrotron Radiat.* **19**, 559–69 (2012).
  53. Kuppenko, I. *et al.* Portable double-sided laser-heating system for Mössbauer spectroscopy and X-ray diffraction experiments at synchrotron facilities with diamond anvil cells. *Rev. Sci. Instrum.* **83**, 124501 (2012).
  54. Aprilis, G. *et al.* Portable double-sided pulsed laser heating system for time-resolved geoscience

- and materials science applications. *Rev. Sci. Instrum.* **88**, 084501 (2017).
55. Prescher, C., McCammon, C. & Dubrovinsky, L. MossA : a program for analyzing energy-domain Mössbauer spectra from conventional and synchrotron sources. *J. Appl. Crystallogr.* **45**, 329–331 (2012).
  56. Dubrovinsky, L. *et al.* The most incompressible metal osmium at static pressures above 750 gigapascals. *Nature* **525**, 226–229 (2015).
  57. Petříček, V., Dušek, M. & Palatinus, L. Crystallographic Computing System JANA2006: General features. *Zeitschrift für Krist. - Cryst. Mater.* **229**, 345–352 (2014).
  58. Sheldrick, G. M. SHELXT – Integrated space-group and crystal-structure determination. *Acta Crystallogr. Sect. A Found. Adv.* **71**, 3–8 (2015).
  59. Sheldrick, G. M. Crystal structure refinement with SHELXL. *Acta Crystallogr. Sect. C Struct. Chem.* **71**, 3–8 (2015).

## Acknowledgments

This work was supported by WWU Münster, the German Research Foundation and the German Federal Ministry of Education and Research. We acknowledge the European Synchrotron Radiation Facility for the provision of synchrotron radiation facilities.

## Author contributions

I.K. initiated and designed the project. I.K., G.A., V.C., and J. J. prepared the high-pressure high-temperature experiments. I. K., D.M.V., G.A., V.C., A.I.C., and C.S.V. conducted the SMS experiments. E.B., M.B., E.K., S.C., and L.D. conducted the X-ray diffraction experiments. I.K. and D.M.V. analyzed the Mössbauer data. E.B. analyzed the X-ray diffraction data. I. K. interpreted the results and wrote the manuscript with contributions from all authors.

## Competing interests

The authors declare no competing interests.

# Figures

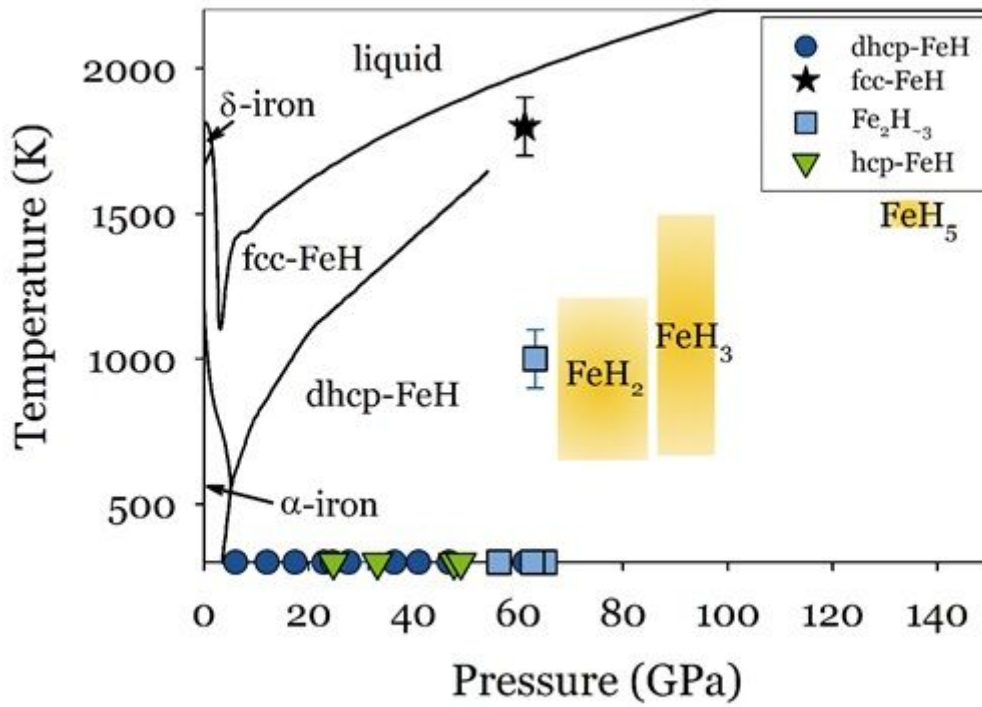
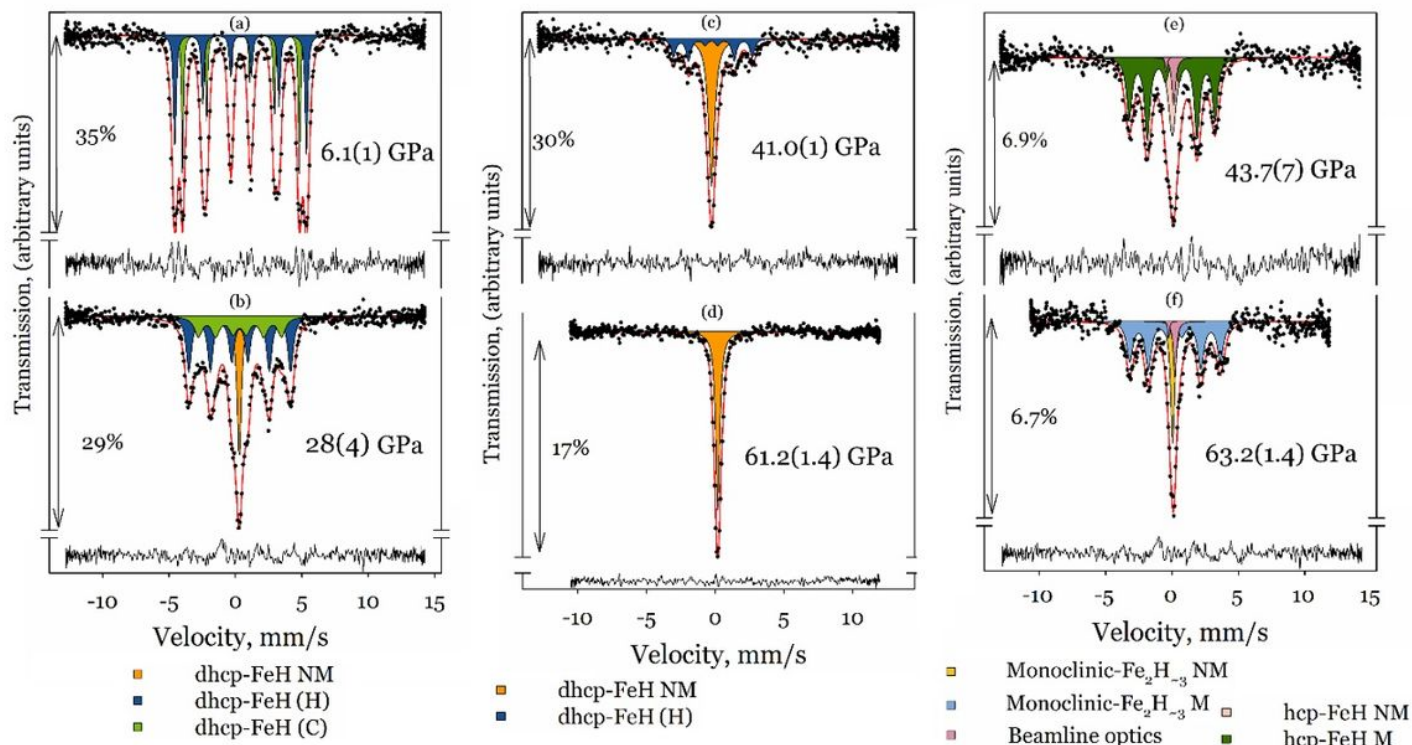


Figure 1

Phase diagram of the Fe-H system. The solid lines are the phase boundaries for the FeH<sub>x</sub> phases with  $x \leq 114, 24, 25$ , the shaded regions are the stability domains of the novel polyhydrides<sup>14,15</sup>. The symbols correspond to the phases investigated in this study, including the two new phases Fe<sub>2</sub>H<sub>-3</sub> and hcp-FeH.



**Figure 2**

Representative SMS spectra of iron hydrides at the indicated pressures and ambient temperature. (a)-(d) – the cold compression of dhcp-FeH; (f) – Fe<sub>2</sub>H<sub>3</sub> synthesized at about 1000 K; (e) hcp-FeH phase obtained upon decompression. Solid lines show the theoretical fits, the percentage bars indicate the relative absorptions, and the residuals of the fits are indicated below each spectrum. M: magnetic; NM: non-magnetic; H and C: hexagonally and cubically close-packed sites respectively.

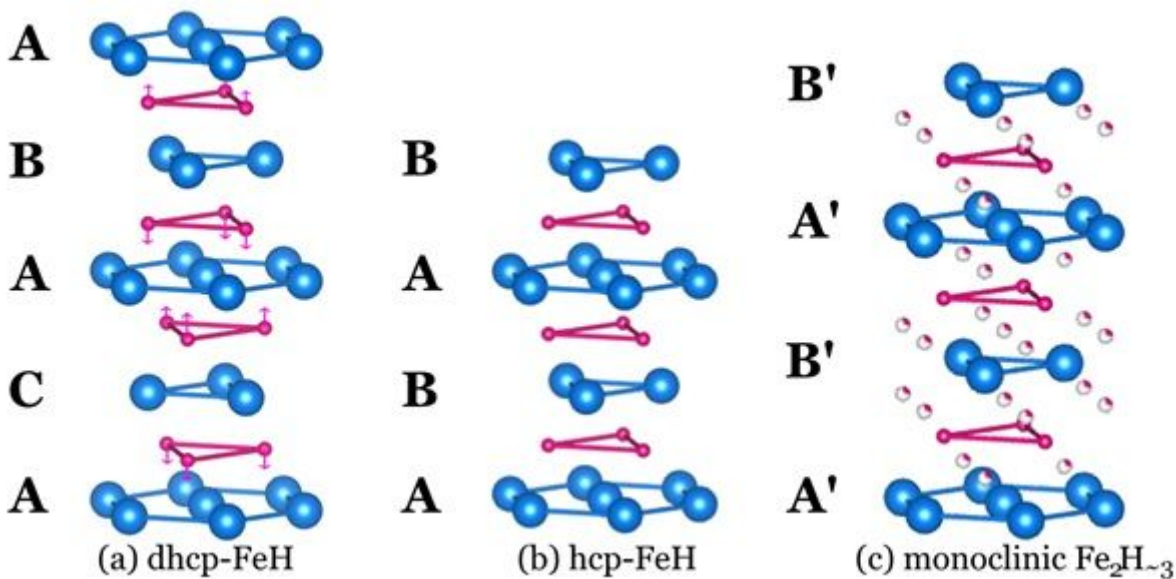


**Figure 3**

The crystal structures of iron hydrides. The blue and pink circles show regular positions of Fe and H atoms, respectively. The arrows indicate the directions of displacements of hydrogen atoms from the centers of octahedral interstices in the dhcp structure. The letters A, B, C represent the standard notation for close-packed layers in the dhcp- and hcp-FeH structures, A' and B' for the distorted close-packed layers in the monoclinic Fe<sub>2</sub>H<sub>~3</sub> structure. In all three structures, all octahedral interstitials are occupied by hydrogen. In Fe<sub>2</sub>H<sub>~3</sub>, additionally, about one-fourth of tetrahedral interstitials are occupied. The structures are visualized using the Vesta 3 software<sup>29</sup>.

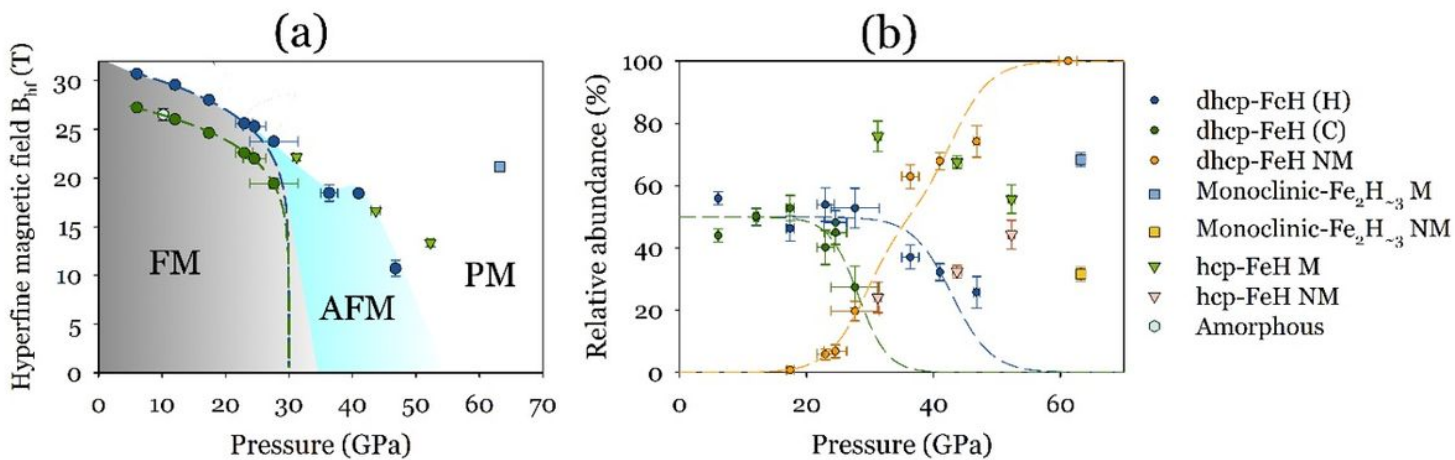


**Figure 4**

Effect of pressure on the hyperfine parameters of iron hydrides at room temperature: (a) hyperfine magnetic field, (b) relative abundance of the components. Dashed lines displayed in (a) are a fit to in the 0-35 GPa range and in (b) are guides for the eyes. The shaded areas in (a) indicate the ferromagnetic (FM), antiferromagnetic (AFM), and paramagnetic (PM) pressure regions for dhcp-FeH. M: magnetic; NM: non-magnetic; H and C: hexagonally and cubically close-packed sites respectively.

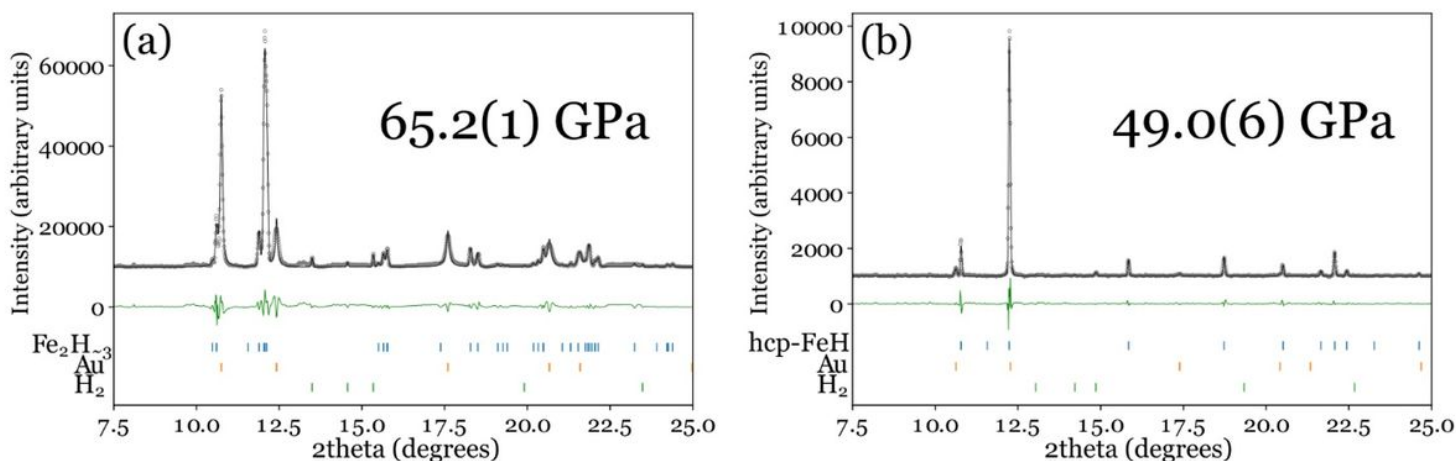


**Figure 5**

X-ray diffraction patterns of (a) monoclinic Fe<sub>2</sub>H<sub>~3</sub> (space group C2/m) and (b) hcp-FeH GPa at indicated pressures and room temperature. Experimental data – grey circles; Le Bail fit – black solid lines;

difference curves – green solid lines. Ticks show predicted positions of the diffraction peaks. The wavelength is 0.4126 Å.

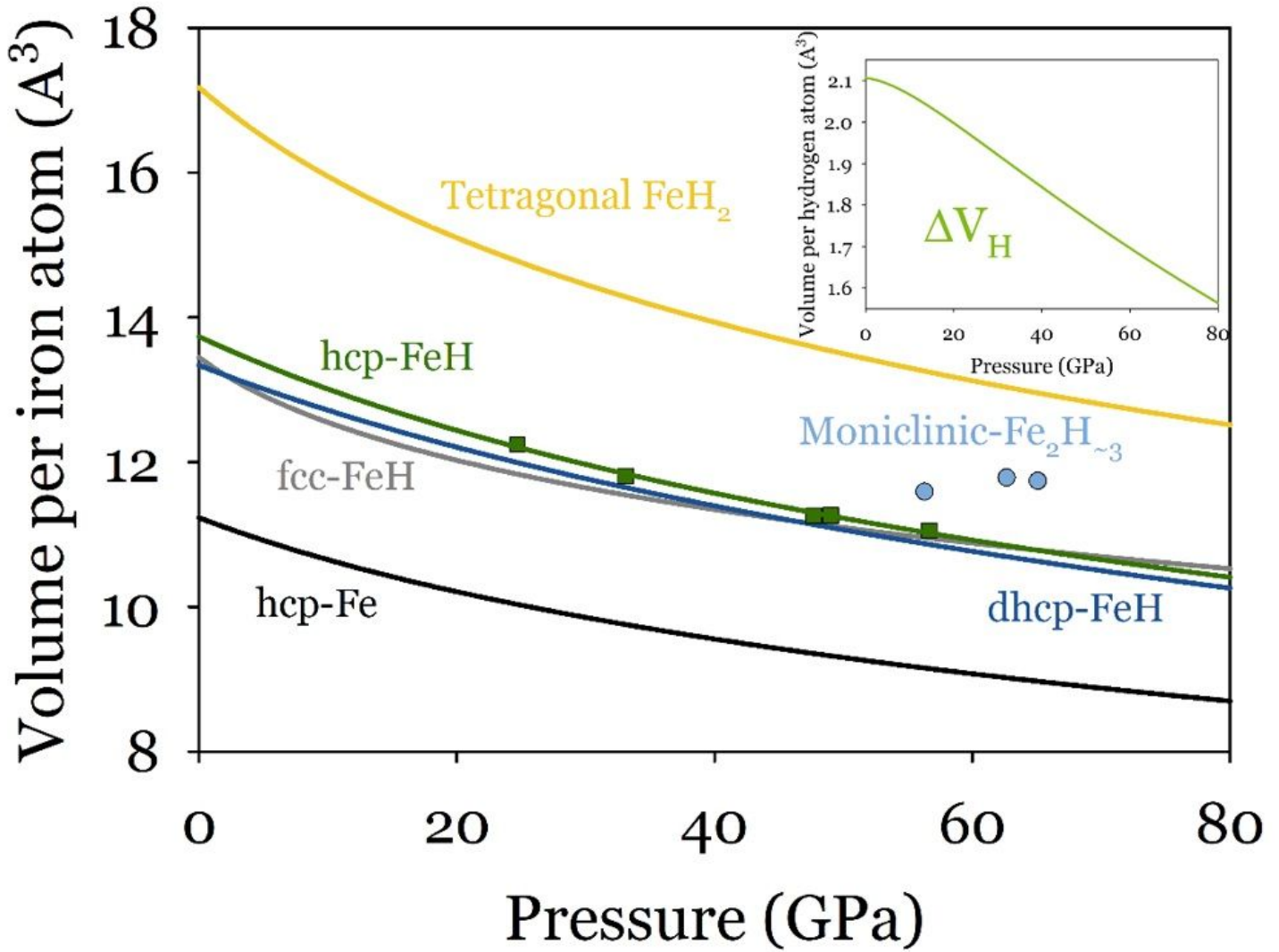


Figure 6

Third-order Birch–Murnaghan equations of state for hcp-FeH (green, this study), hcp-Fe (black)<sup>35</sup>, dhcp-FeH (blue), and tetragonal  $\text{FeH}_2$  (yellow)<sup>14</sup>, together with P-V data for monoclinic- $\text{Fe}_2\text{H}_{\sim 3}$  (light-blue circles). Error bars do not exceed the size of the symbols. The EOS parameters are given in Supplementary Table 3. The inset shows the calculated atomic volume expansion caused by the incorporation of one atom of interstitial hydrogen according to Eq. (1).

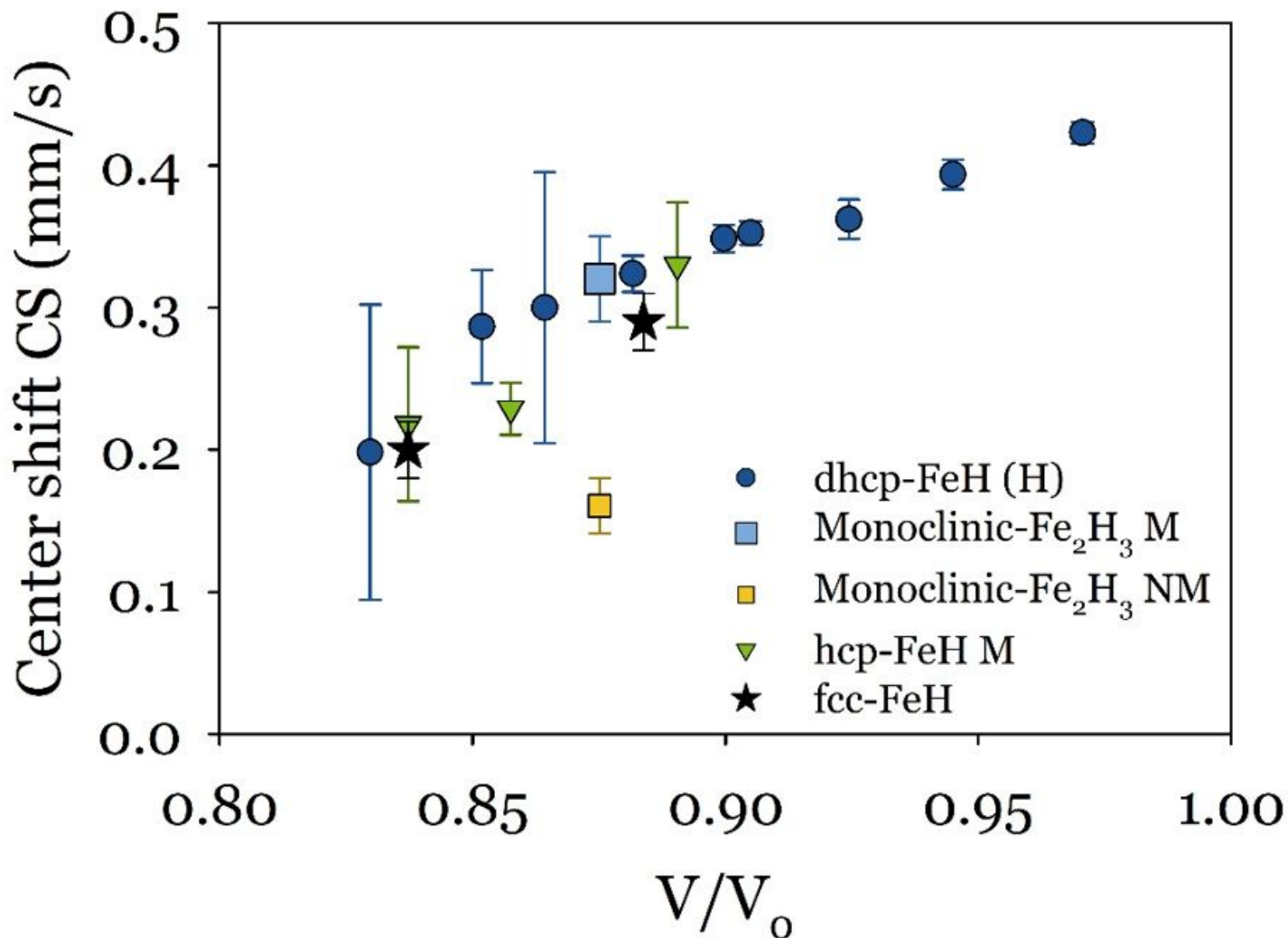


Figure 7

Volume dependence of the center shift in dhcp-FeH (blue), hcp-FeH (green), and monoclinic Fe<sub>2</sub>H<sub>3</sub>. The effect of volume increase well explains the higher CS of the magnetic component in Fe<sub>2</sub>H<sub>3</sub> (light blue) but does not explain the low-CS of the nonmagnetic component (yellow). Volumes of dhcp-FeH are calculated using the EoS parameters reported in Supplementary Table 2. The data for fcc-FeH are from 21.

## Supplementary Files

This is a list of supplementary files associated with this preprint. Click to download.

- [20210114FehydridesKupenkoEtAlfinalSM.docx](#)